

THESIS FOR THE DEGREE OF LICENTIATE OF ENGINEERING

---

# Optical remote sensing of industrial gas emission fluxes

---

**John Johansson**



**CHALMERS**

*Department of Earth and Space Sciences*  
CHALMERS UNIVERSITY OF TECHNOLOGY  
Göteborg, Sweden 2013

Optical remote sensing of industrial gas emission fluxes  
JOHN JOHANSSON

© JOHN JOHANSSON, 2013

Technical Report 60L

Department of Earth and Space Sciences  
Chalmers University of Technology  
SE-412 96 Göteborg, Sweden  
Phone: +46 (0)31-772 1000

Printed in Sweden  
Chalmers Reproservice  
Göteborg, Sweden 2013

**Contact information:**

John Johansson  
Department of Earth and Space Sciences  
Chalmers University of Technology  
Hörsalsvägen 11  
SE-412 96i Göteborg, Sweden

Phone: +46 (0)31-772 5655  
Fax: +46 (0)31-772 3663  
Email: john.johansson@chalmers.se

Last updated on July 29, 2013.



This work is licensed under the *Creative Commons Attribution 3.0 License*.

Typeset in L<sup>A</sup>T<sub>E</sub>X

# Optical remote sensing of industrial gas emission fluxes

John Johansson

*Optical Remote Sensing, Department of Earth and Space Sciences  
Chalmers University of Technology*

## Abstract

Mobile optical remote sensing techniques offer promising possibilities to quantify and geographically attribute local industrial gaseous emissions to the atmosphere. Studies have repeatedly shown that such emissions are often poorly understood, underestimated, and thereby not properly accounted for in emission inventories and regional atmospheric chemistry models, especially for emissions of VOCs. A better understanding and quantification of industrial VOC emissions is crucial for combating ground-level ozone, a serious problem facing most of the world's larger urban areas.

This thesis presents results from a number of measurement campaigns primarily conducted in the area around Houston, Texas, USA, which has one of the world's largest concentrations of oil, gas and petrochemical industries. In the campaigns, the two flux measurement methods Solar Occultation Flux (SOF) and Mobile DOAS were used to quantify emissions of VOCs (alkanes and alkenes), SO<sub>2</sub>, NO<sub>2</sub>, and formaldehyde (HCHO) from the largest industrial conglomerates in the area.

Measured emissions are compared to industry estimates reported to emission inventories, showing discrepancies of up to an order of magnitude for VOCs but not for SO<sub>2</sub> and NO<sub>2</sub>. Emission factor models are used to estimate effects on VOC emissions of unrepresentative meteorological conditions during the measurement campaigns. These effects are determined to be too small to explain the discrepancies between measurements and reported emissions seen for VOCs.

A plume chemistry model is applied to a number of cases where formaldehyde were detected together with significant amounts of alkenes in order to assess whether the formaldehyde could be explained as a secondary pollutant from the oxidation of alkenes. The results of the modeling shows that secondary emissions can only explain a small fraction of the measured formaldehyde flux in most cases, suggesting that most of the formaldehyde emissions measured from local sources were primary emissions. Secondary emissions are, however, still believed to be the largest source of formaldehyde further downwind from sources.

**Keywords:** optical remote sensing, absorption spectroscopy, solar occultation, FTIR, DOAS, VOC, formaldehyde, gas emission, flux measurement



## List of appended papers

This thesis is a summary of the following three papers. References to the papers will be made using roman numerals.

Paper I – J. Mellqvist, J. Samuelsson, **J. K. E. Johansson**, C. Rivera, B. Lefer, S. Alvarez, J. Jolly,  
Measurements of industrial emissions of alkenes in Texas using the solar occultation flux method,  
*Journal of Geophysical Research*, vol. 115, no. D17, p. D00F17

Paper II – **J. K. E. Johansson**, J. Mellqvist, J. Samuelsson, B. Offerle, J. Moldanova, B. Rappenglück, B. Lefer, J. Flynn,  
Quantitative measurements and modeling of industrial formaldehyde emissions in the Greater Houston area during campaigns in 2009 and 2011,  
*Journal of Geophysical Research*, (submitted)

Paper III – **J. K. E. Johansson**, J. Mellqvist, J. Samuelsson, B. Offerle, B. Lefer, B. Rappenglück, J. Flynn, G. Yarwood,  
Emission measurements of alkenes, alkanes, SO<sub>2</sub> and NO<sub>2</sub> from stationary sources in Southeast Texas over a 5-year-period using SOF and Mobile DOAS,  
*Journal of Geophysical Research*, (submitted)

## Other contributions (not included)

This is a list of conference contributions and non-peer reviewed articles.

- A – J. Mellqvist, **J. K. E. Johansson**, J. Samuelsson, C. Rivera, B. Lefer, S. Alvarez,  
Comparison of Solar Occultation Flux measurements to the 2006 TCEQ emission inventory and airborne measurements for the TexAQS II, *TERC report project H53, 2008*,  
[http://www.tceq.texas.gov/assets/public/implementation/air/am/contracts/reports/da/20081108-comparison\\_solar\\_occultation\\_flux\\_measurements.pdf](http://www.tceq.texas.gov/assets/public/implementation/air/am/contracts/reports/da/20081108-comparison_solar_occultation_flux_measurements.pdf)
- B – J. Mellqvist, **J. K. E. Johansson**, J. Samuelsson, B. Offerle, B. Rappenglück, C.-S. Wilmot, R. Fuller,  
Investigation of VOC radical sources in the Houston area by the Solar Occultation Flux (SOF) method, mobile DOAS (SOF-II) and mobile extractive FTIR ,  
*TERC report project H-102, 2010*,  
<http://files.harc.edu/Projects/AirQuality/Projects/H102/H102FinalReport.pdf>
- C – **J. K. E. Johansson**, J. Mellqvist, J. Samuelsson, B. Offerle, B. Rappenglück,  
Investigation of VOC radical sources in the Houston Area by the Solar Occultation Flux (SOF) method and Mobile DOAS,  
*AGU Conference 2010, (poster), San Fransisco, CA, USA*
- D – **J. K. E. Johansson**, J. Mellqvist, J. Samuelsson, B. Offerle, B. Rappenglück, D. Anderson, B. Lefer, S. Alvarez, J. Flynn,  
Quantification of industrial emissions of VOCs, NO<sub>2</sub> and SO<sub>2</sub> by SOF and Mobile DOAS,  
*AQRP report project 10-006, 2011*,  
<http://aqrp.ceer.utexas.edu/projectinfo/10-006/10-006%20Final%20Report.pdf>
- E – **J. K. E. Johansson**, J. Mellqvist, B. Lefer, J. Flynn,  
SOF HRVOC emission study at Longview, Texas,  
*NETAC report, 2012*,  
[http://www.etcog.org/UserFiles/File/NETAC/NETAC\\_SOF\\_rev.pdf](http://www.etcog.org/UserFiles/File/NETAC/NETAC_SOF_rev.pdf)

## Acknowledgements

I would like to start by taking the opportunity to express my sincere gratitude to all the people, without whom the work behind this thesis would not have been possible, or at least not as rewarding. Although listing everybody would be unpractical, the following people deserve a special mention.

All the colleagues in the Optical remote sensing group, for their help with instruments, theoretical questions, computer issues, and for sharing their knowledge and experience. Among them, especially my supervisor Dr. Johan Mellqvist, for organizing field studies, for teaching me about spectroscopy and atmospheric science, and for guiding me through the jungle of writing papers.

My second set of colleagues at Fluxsense AB, for keeping the knowledge about SOF measurements alive between the campaigns, and for teaching it to me over and over again. Special thanks to Jerker Samuelsson and Brian Offerle, who have participated and played major roles in all of the measurement campaigns which this thesis is based on.

All the people at the University of Houston who have participated in the measurements, for their assistance and patience. Especially Dr. Barry Lefer and Dr. Bernhard Rappenglück, for organizing the campaigns, and James Flynn, for custom building measurement vehicles and solving our technical problems.

Last but not necessarily least, Andreas Skyman, for providing the Latex template for this thesis and for painstakingly proofreading its content, thereby sparing all subsequent readers the eyesore of numerous instances of improper grammar, ambiguous phrases, confused rambling, and split infinitives. Marcus Billeter and Ludde Edgren also deserve credit for providing the precursors to Andreas's Latex template.



# Table of contents

## I Summary

<b>1 Introduction</b>	<b>1</b>
1.1 Photochemical smog . . . . .	1
1.2 Ground-level ozone in Houston . . . . .	5
<b>2 Optical remote sensing</b>	<b>7</b>
2.1 Absorption spectroscopy . . . . .	8
2.2 Flux measurements . . . . .	9
2.3 Solar Occultation Flux . . . . .	13
2.4 Mobile DOAS . . . . .	16
2.5 Wind measurements . . . . .	19
2.5.1 GPS radiosondes . . . . .	20
2.5.2 Ground-based wind masts . . . . .	21
2.5.3 Remote sensing wind profilers . . . . .	21
2.6 Error analysis . . . . .	22
2.6.1 Spectroscopic errors . . . . .	22
2.6.2 Wind measurement errors . . . . .	23
2.6.3 Other error sources . . . . .	25
2.6.4 Composite flux measurement error . . . . .	26
<b>3 Summary of papers</b>	<b>29</b>
3.1 Measurements of industrial emissions of alkenes in Texas using the solar occultation flux method . . . . .	29
3.2 Quantitative measurements and modeling of industrial formaldehyde emissions in the Greater Houston area during campaigns in 2009 and 2011 . . . . .	30
3.3 Emission measurements of alkenes, alkanes, SO <sub>2</sub> and NO <sub>2</sub> from stationary sources in Southeast Texas over a 5-year-period using SOF and Mobile DOAS . . . . .	32
<b>Bibliography</b>	<b>35</b>

<b>II Appended papers</b>	<b>41</b>
<b>Paper I</b> – Measurements of industrial emissions of alkenes in Texas using the solar occultation flux method	<b>43</b>
<b>Paper II</b> – Quantitative measurements and modeling of industrial formaldehyde emissions in the Greater Houston area during campaigns in 2009 and 2011	<b>59</b>
<b>Paper III</b> – Emission measurements of alkenes, alkanes, SO <sub>2</sub> and NO <sub>2</sub> from stationary sources in Southeast Texas over a 5-year-period using SOF and Mobile DOAS	<b>95</b>

**Part I**

**Summary**



# 1

## Introduction

### 1.1 Photochemical smog

Photochemical smog is the common name of an atmospheric chemical process primarily associated with urban areas, which constitutes a serious threat to the environment, human health and economic interests. This process is responsible for a host of secondary pollutants, several of which are associated with negative effects, but the most prominent and well known is probably tropospheric ozone, or ground-level ozone. Ozone,  $O_3$ , occurs naturally in high concentrations in the stratosphere due to photolysis of molecular oxygen,  $O_2$ , by ultraviolet radiation from the sun. The set of reactions regulating the stratospheric ozone concentration is known as the Chapman cycle:



Photolysis of  $O_2$ , the necessary first step for ozone production in this process, requires ultraviolet light with wavelengths shorter than 250 nm. Light in this wavelength region is available in the stratosphere, but it does not reach the ground due to the absorption by all the  $O_3$  and  $O_2$  above. In fact, the absorption by stratospheric  $O_3$  prevent virtually all ultraviolet radiation below 290 nm from reaching ground. This is a crucial condition for all land-based life on

Earth, but also explains why the Chapman cycle is the dominant ozone formation mechanism in the stratosphere, but not in the troposphere.

In the troposphere, the major source of ozone production is instead the photolysis of  $\text{NO}_2$ . This photolysis only requires light of wavelengths below 430 nm, which reaches the troposphere in significant quantities during daytime, especially in clear conditions. In the presence of nitrogen oxides,  $\text{NO}$  and  $\text{NO}_2$ , collectively referred to as  $\text{NO}_x$ , the tropospheric ozone concentration is largely governed by the following reactions:



This reaction system is visualized in figure 1.1, where each species is represented by a circle and the reactions are represented by arrows between the circles. This figure illustrates how  $\text{NO}_x$  cycles back and fourth between  $\text{NO}_2$  and  $\text{NO}$ , while oxygen cycles back and fourth between  $\text{O}_2$  and  $\text{O}_3$ . These two cycles are coupled through reaction (1.8). For a given set of photolysis rates and a given  $\text{NO}_x$  concentration, the concentrations of  $\text{O}_3$ ,  $\text{O}$ ,  $\text{NO}_2$  and  $\text{NO}$  will reach an equilibrium fairly quickly. Since an  $\text{NO}$  molecule is produced in the photolysis of  $\text{NO}_2$ , together with each free  $\text{O}$  atom needed to produce  $\text{O}_3$ , and since  $\text{NO}$  is so reactive with  $\text{O}_3$ , equilibrium concentrations of  $\text{O}_3$  can never reach particularly high levels in this system. To achieve higher ozone concentration reaction (1.8) needs to be bypassed by some other, even faster reaction turning  $\text{NO}$  back to  $\text{NO}_2$ , thereby decoupling the  $\text{NO}_x$  cycle from the  $\text{O}_2$ - $\text{O}_3$  cycle, allowing continuous  $\text{O}_3$  production without equally fast destruction by  $\text{NO}$ . In photochemical smog, this bypassing is the result of the oxidation of organic molecules.

Volatile Organic Compounds (VOCs) is a term used to refer to organic molecules that are volatile enough at ambient temperatures to have significant evaporation, allowing them to play a role in atmospheric chemistry. Anthropogenic sources of VOCs are typically of greatest importance for photochemical smog, but biogenic sources can dominate in rural areas. Both industry and motor vehicles are large anthropogenic sources of VOC emissions, but the origin of the VOCs is generally oil and natural gas, regardless of the source. The most important oxidant for VOCs in the atmosphere is the hydroxyl radical,  $\text{OH}$ . If the molecule  $\text{RCH}_3$ , where  $\text{R}$  is an arbitrary carbon chain or other functional group, is taken to represent a typical VOC, a typical oxidation step of it can be described like this. First the VOC molecule reacts with a hydroxyl radical:

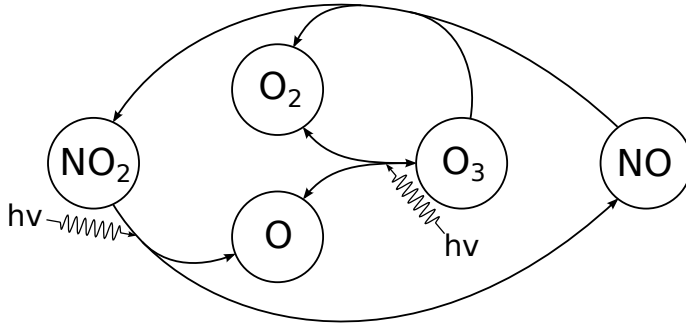
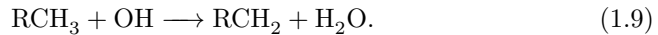
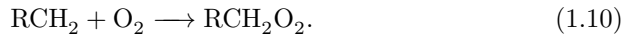


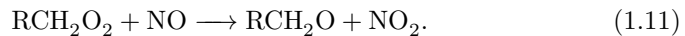
**Figure 1.1:** *The reaction system regulating tropospheric ozone concentration in the presence of  $\text{NO}_x$  and sun light. Circles represent molecular species and arrows represent reactions between them.*



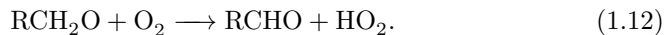
The hydroxyl radical takes a hydrogen atom from the VOC molecule, producing an organic radical and a water molecule. The organic radical then reacts with an oxygen molecule to form a peroxyradical:



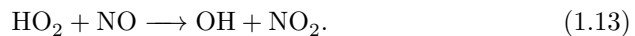
The peroxyradical reacts with an NO, which takes one oxygen atom to form  $\text{NO}_2$ , thereby bypassing the  $\text{NO}-\text{O}_3$  reaction as explained above:



The resulting oxyradical reacts with an oxygen molecule, which takes a hydrogen atom and forms a hydroperoxyl radical,  $\text{HO}_2$ , and an aldehyde:



The hydroperoxyl radical reacts with another NO to form  $\text{NO}_2$  and a hydroxyl radical, replacing the one consumed in the first oxidation step:



If the reactions (1.9)–(1.13) are combined, the resulting net reaction becomes:



Of course, far from all VOCs are on the form  $\text{RCH}_3$ , and even if they were, there are many other possible reaction paths than the one described here. However, the net reaction (1.14) still captures the general broad pattern for the oxidation of most VOCs pretty well. Hydrogen atoms on the VOCs are gradually replaced by oxygen atoms, while at the same time oxidizing  $\text{NO}$  to  $\text{NO}_2$ . The oxidation is dependent on  $\text{OH}$  radicals, but they are for the most part not consumed in the process. The total number of radicals is conserved by most reaction steps in the oxidation process, but they cycle through the forms of hydroxyl radicals, hydroperoxyl radicals, and different forms of organic radicals. There are several sources of the hydroxyl radicals needed for oxidation of VOCs, but one of the most important is the photolysis of  $\text{O}_3$ . The free oxygen atom formed from this photolysis is in an excited state,  $\text{O}({}^1\text{D})$ , which allows it to react with a water molecule to form two hydroxyl radicals:



This is one of several ways in which the photochemical smog chemistry generates the hydroxyl radicals needed to keep it going. There are of course also reactions causing losses of radicals, but the fact that the process creates its own radicals means that the necessary prerequisites for photochemical smog formation are just  $\text{NO}_x$ , VOCs and sun light. In terms of ground-level ozone formation, the  $\text{NO}_x$  and the sun light can be thought of as producing the ozone, while the VOCs prevent the ozone from being consumed as fast as it is produced. Even though these are the only prerequisites for photochemical smog, there many other factors influencing the severity, most notably perhaps the meteorology.

Although all VOCs contribute to photochemical smog, alkenes are often of particular interest. Even though emissions of alkanes are typically much larger than alkene emissions, alkene can still dominate the ozone formation because they have higher  $\text{OH}$  reactivity. The higher  $\text{OH}$  reactivity of alkenes also gives them a typical lifetime that is better matched to the typical lifetime of  $\text{NO}_x$ . A polluted air mass may often run out of  $\text{NO}_x$  before much of the alkanes have had time to be oxidized. Alkenes are also involved in two of the other major ways in which photochemical smog produces its own hydroxyl radicals. One is through ozonolysis, in which alkenes react with ozone forming  $\text{OH}$  in varying amounts. The other way is through the production of formaldehyde ( $\text{HCHO}$ ), which is produced in high yields from the oxidation of many alkenes. Photolysis of the formaldehyde results in the formation of  $\text{HO}_2$  radicals, which in the presence of  $\text{NO}$  will be converted to  $\text{OH}$  through reaction (1.13). By contributing to the formation of  $\text{OH}$ , alkenes also speed up the oxidation of VOCs. Additionally, the

production of OH from the photolysis of formaldehyde makes any primary emission sources of formaldehyde especially interesting. Primary emissions would make formaldehyde available early in the morning, before the photochemical smog has started, and the OH produced from its photolysis could speed up the photochemistry faster.

8-Hour Ozone Nonattainment Areas (2008 Standard)

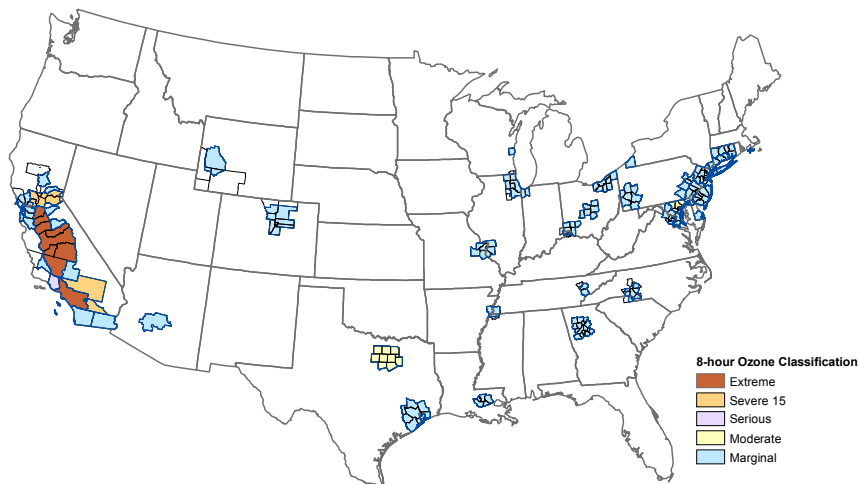


Image: USEPA

**Figure 1.2:** Areas in USA classified in 2012 as nonattainment areas under the current 8 hour ozone standard.

## 1.2 Ground-level ozone in Houston

In the USA, ground-level ozone is regulated by the Clean Air Act, which requires USEPA (United States Environmental Protection Agency) to set National Ambient Air Quality Standards (NAAQS) for harmful pollutants. The current ozone standard from 2008 requires that the annual fourth-highest daily maximum 8 hour concentration of ozone, averaged over a three year period, does not exceed 75 parts per billion (ppb). Areas that fail to meet this criterion are classified as nonattainment areas, requiring them to implement plans to reduce ozone levels until they meet the standard. Figure 1.2 shows a map over the areas in USA classified as nonattainment areas. Evidently, most of the major metropolitan areas and their surroundings are nonattainment areas.

Houston, Texas is not the worst nonattainment area, but it is special in the sense that it has the country's highest concentration of oil, gas and petrochemical industries. For this reason, industrial emissions of VOCs play a particularly large role in photochemical smog formation here. Studies within the 2000 TexasAQS

(Texas Air Quality Study) and the 2006 TexaAQS II indicated that emission inventories drastically underestimate industrial VOC emissions in Houston [1–8]. Several also concluded that these emissions significantly contribute to ozone formation [2, 4, 6, 8–10].

Additionally, the contribution of different VOCs to ozone formation was studied and the general pattern was that ethene ( $C_2H_4$ ), propene ( $C_3H_6$ ), formaldehyde (HCHO) and acetaldehyde ( $CH_3CHO$ ) were the largest contributors [2, 7, 9]. Since the oxidation of ethene and propene produces formaldehyde and acetaldehyde, emissions of ethene and propene might alone explain this situation. This view is supported by some studies [8, 11], while others have found indications of significant primary emission sources of formaldehyde [12–14].

# 2

## Optical remote sensing

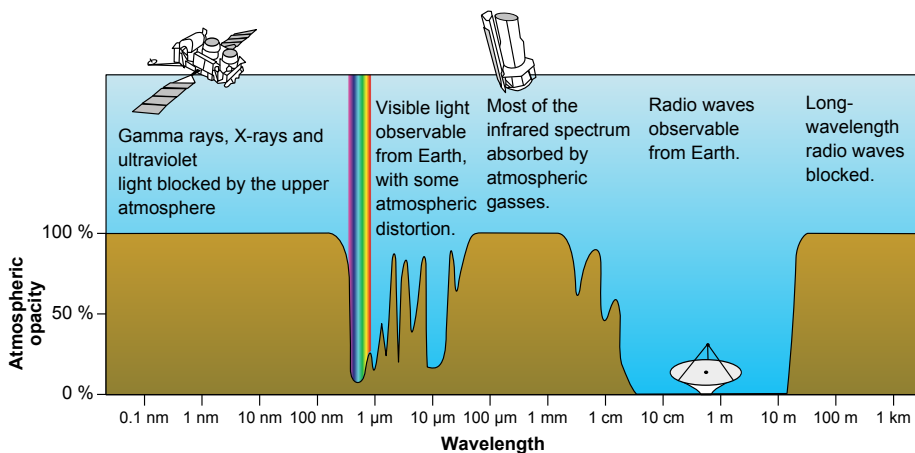


**Figure 2.1:** The opacity of Earth's atmosphere to electromagnetic radiation as a function of wavelength. Through most of electromagnetic spectrum, the atmosphere transmits very little radiation.

We humans tend to think of the atmosphere as completely transparent. This is because it almost is in the wavelength region that our eyes are sensitive to. In clear conditions we can see the sun, the moon and the stars from earth with nearly the same intensity as we would from outer space, even though the light has to pass through kilometers of atmosphere before it can reach our eyes. This property is by no means typical throughout the electromagnetic spectrum. Figure 2.1 shows the opacity of the atmosphere (the fraction of light absorbed) to electromagnetic radiation as a function of wavelength. As shown, there are

basically two windows where radiation passes through the atmosphere. One spans the short radio waves and large parts of the microwave region, while the other stretches from the mid infrared to the long ultraviolet. The first window is more distinctly transparent while the second one has large variations in opacity within it. Outside these two windows the atmosphere blocks virtually all electromagnetic radiation.

The absorption pattern in figure 2.1 is the combined effect of the absorption pattern of all the molecular constituents of the atmosphere, although the major features are almost entirely dominated by a few important species: carbon dioxide, oxygen, ozone and water vapor. How much radiation is absorbed and for which wavelengths are unique characteristics for each molecular species, which depend on the energy levels available for excitation in the molecules. Absorption in the microwave region generally corresponds to excitations of rotational energy levels, while the infrared corresponds to combinations of rotational and vibrational excitations, the visible and ultraviolet to excitations of valence electrons, and X-ray and gamma ray to excitations of tighter bound electrons.

Molecular absorption of electromagnetic radiation is generally described by the Beer–Lambert law. Ignoring scattering phenomena this law can be written:

$$I_1(\lambda) = I_0(\lambda) \exp \left( - \sum_i \int_P n_i(\mathbf{x}) \sigma_i(\lambda, T, p) dl \right), \quad (2.1)$$

where  $I_0(\lambda)$  is the intensity of light as a function of wavelength  $\lambda$  before passing through an air mass and  $I_1(\lambda)$  is the same intensity after having passed through the air mass.  $n_i(\mathbf{x})$  is the number density of molecular species  $i$  at point  $\mathbf{x}$  and  $\sigma_i(\lambda, T, p)$  is the absorption cross section of  $i$  at wavelength  $\lambda$ , which is also temperature and pressure dependent. The integral is a path integral over the path of the light,  $P$ , through the air mass and the sum is of all absorbing molecular species in the air mass. The absorption cross section of each molecular species consist of a set of discrete absorption lines, each corresponding to a transition between two energy levels of the molecule. The widths of the absorption lines are caused by Doppler broadening and collision-induced broadening, which are temperature and pressure dependent. Despite the broadening, the discrete nature of the absorption lines causes cross section features that vary greatly over short wavelength intervals and are unique to each molecule. This property makes it possible to separate the different terms in the sum in equation (2.1) and to distinguish them from other phenomena affecting the light intensity, like scattering.

## 2.1 Absorption spectroscopy

Equation (2.1) can be rewritten:

$$-\log\left(\frac{I_1(\lambda)}{I_0(\lambda)}\right) = \sum_i \int_P n_i(\mathbf{x})\sigma_i(\lambda, T, p) dl. \quad (2.2)$$

If the variations in temperature and pressure within the air mass can be assumed to be small,  $\sigma_i(\lambda, T, p)$  will not vary significantly with position and equation (2.2) can be written:

$$-\log\left(\frac{I_1(\lambda)}{I_0(\lambda)}\right) = \sum_i C_i\sigma_i(\lambda, T, p), \quad (2.3)$$

where  $C_i$  is the concentration column (or just column) of species  $i$  along the light path, defined as:

$$C_i = \int_P n_i(\mathbf{x}) dl. \quad (2.4)$$

Equation (2.3) is linear in the  $C_i$  variables. If  $I_1(\lambda)$  and  $I_0(\lambda)$  are measured with sufficient accuracy and spectral resolution in a wavelength region and  $\sigma_i(\lambda, T, p)$  is known for all species relevant in this region, the equation can be solved for the  $C_i$ :s. This is the principle for how most basic absorption spectroscopy is performed. Typically, the cross sections need to be degraded to the resolution of the measurements by convolving them with the instrument function and a polynomial in  $\lambda$  might be added to the right hand side of equation (2.3) to account for scattering and other possible effects that vary slowly with wavelength compared to the cross sections. A method like this to determine columns from measured spectra is called a spectral retrieval routine or spectral fitting routine. Under certain assumptions, as described above, this method can be reduced to solving an over-determined linear system of equations using a linear least-squares method. However, for some applications these assumptions do not hold and a more advanced spectral retrieval routine is needed. For measurements of entire vertical atmospheric columns, for instance, the large variations in temperature and pressure throughout the atmosphere, and their effect on the cross sections, need to be taken into account. This can be done by creating a forward model based on equation (2.1) and fitting the parameters of that model to a measured spectrum  $I_1(\lambda)$  using a non-linear optimization method. How to design and parametrize the forward model and what optimization method to use depend on the particular application.

## 2.2 Flux measurements

Spectroscopic retrieval, as described above, typically gives results in the form of columns. A column is a path integral of a concentration (or number density or similar) along a light path. If the concentration is constant along the path, the

column is the concentration multiplied by the path distance. In many spectroscopic applications, the quantity of interest is a concentration. For example, the concentrations of a number of species might be tracked in a laboratory reactor cell by making spectroscopic measurements along a fixed path in it. The spectroscopic retrieval of the measured spectra gives columns and concentrations are obtained by dividing the column by the fixed path length. If the concentration is not homogeneous in the cell, this will give an average of the concentration along the light path.

For the purpose of measurements of gas fluxes, however, there is a great advantage to measuring columns instead of just concentrations. The mass flux  $\dot{m}_i$  of species  $i$  through a surface  $S$  in the atmosphere can be written as a surface integral:

$$\dot{m}_i = \iint_S \rho_i(\mathbf{v} \cdot \mathbf{n}) dA, \quad (2.5)$$

where  $\rho_i$  is the mass density of the species,  $\mathbf{v}$  is the wind velocity vector and  $\mathbf{n}$  is the normalized vector normal to the surface. The mass density is of course proportional to the number density  $n_i$  of the same species:  $\rho_i = M_i n_i / N_a$  where  $M_i$  is the molar mass of the species and  $N_a$  is the Avogadro constant. If you want to calculate the surface integral of a quantity, it is a great convenience to be able to directly measure the integral of that quantity along one dimension. In Solar Occultation Flux (SOF) and Mobile DOAS (Differential Optical Absorption Spectroscopy), the two flux measurement methods that will be presented below, spectroscopic measurements are made using an instrument in a measurement vehicle along an open light path from the instrument to the sky. As the vehicle moves on the ground, the light path slices through the atmosphere, forming a surface. Assuming that the direction of the light path remains constant as the vehicle moves, the surface integral in equation (2.5), with this surface as  $S$ , can be written:

$$\dot{m}_i = \int_V \left[ \int_P \rho_i dl \right] \mathbf{v} \cdot (\hat{\mathbf{z}} \times d\mathbf{x}), \quad (2.6)$$

where  $P$  is the measurement light path,  $V$  is the path driven by the vehicle and  $\hat{\mathbf{z}}$  is a normalized vector in the direction of the measurement path. Using the proportionality of mass and number density and the definition in equation (2.4), the inner integral can be written:

$$\int_P \rho_i dl = \int_P \frac{M_i}{N_a} n_i dl = \frac{M_i}{N_a} C_i, \quad (2.7)$$

which allows equation (2.6) to be written:

$$\dot{m}_i = \frac{M_i}{N_a} \int_V C_i \mathbf{v} \cdot (\hat{\mathbf{z}} \times d\mathbf{x}). \quad (2.8)$$

Since  $C_i$  is given by the spectral retrieval for the species possible to measure with the instrument, only the outer integral along the ground path needs to be addressed. Since each spectral measurement takes a finite amount of time, the spectral retrieval will give a discrete series of  $C_i$ :s for each species. Hence, the integral has to be approximated by a sum. Since horizontal movement typically dominates for a ground vehicle,  $d\mathbf{x}$  can be assumed to be in the horizontal plane. For this reason, only the angle between the light path and zenith matters for the cross product with  $\hat{\mathbf{z}}$ . Furthermore, since the horizontal wind component typically dominates over the vertical component, and since  $\hat{\mathbf{z}}$  is fairly close to vertical in most measurements, the vertical wind component can typically be neglected. Using these assumptions, equation (2.8) can be approximated by:

$$\dot{m}_i = \frac{M_i}{N_a} \sum_j C_{ij} v_j \cos(\theta_j) \sin(\alpha_j) d_j, \quad (2.9)$$

where  $C_{ij}$  is the column of species  $i$  retrieved from spectrum  $j$  in a measurement series,  $v_j$  is the wind speed at that time,  $\theta_j$  is the angle of the light path from zenith,  $\alpha_j$  is the angle between the wind direction and driving direction, and  $d_j$  is the distance travelled during the measurement of the spectrum. This is the formula that is typically used for flux calculations in SOF and Mobile DOAS. In addition to the spectral measurements, the position of the vehicle needs to be logged carefully with a GPS-receiver to calculate  $d_j$  and the driving direction, and some form of wind data is needed. Wind measurements are discussed in section 2.5.

Equation (2.9) in theory applies to any column measurements from a vehicle along any conceivable measurement path driven. For the purpose of measuring emission fluxes from local sources, certain specific measurement strategies are typically used. First of all, the spectroscopic retrieval is typically made relative to a reference spectrum measured in a location assumed to be free from local emissions. The evaluated columns from such a retrieval are not absolute, but relative to the background column present in the reference spectrum. This is called a differential measurement. This is partly motivated because differential spectral evaluations are typically easier to make and more precise. But the differential column is also the relevant quantity for calculating the flux from a local source. Figure 2.2 illustrates how a typical flux measurement is made nearby a local industrial facility. The differential column is measured continuously while driving along a road downwind of the industry. Before and after intercepting the plume, the evaluated column remains fairly constant around zero. As the path of the measured light cuts through the plume, the evaluated column of the species measured rises to a peak value and then goes back down to zero. The

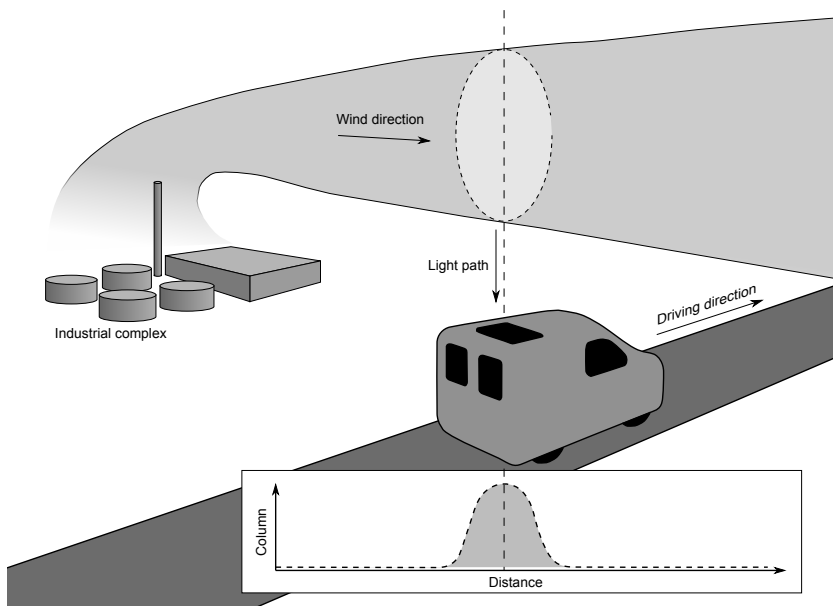


**Figure 2.2:** Illustration of the principles of flux measurements in an industrial plume. The plume appears as a peak a peak in the series of measured columns on top of an ideally constant background. The area under the peak, multiplied by the wind speed and geometric corrections, corresponds to the flux in the plume of the species measured.

area under the peak multiplied by the wind speed and geometrical corrections gives the flux in the plume. If there are variations in the background concentration, the evaluated column might not stay constant at zero before and after the plume. In such cases it is important to determine a baseline that matches the column right before and after passing the plume and to include only the area above that baseline. If the background concentration varies too much or over too short distances, it will be difficult to separate the plume from the background variations, increasing the uncertainty of the flux measurement or even making it useless.

Downwind measurements are typically combined with similar upwind measurements. If there are no significant emission sources close-by on the upwind side, only one or a couple of measurements is typically needed to verify this. If significant upwind sources exist, the incoming flux from these sources needs to be measured regularly to be subtracted from the flux downwind of the source of interest. If the upwind sources are large compared to the downwind source, the accuracy will be worse for this difference between the two fluxes. If possible, the measurements of emissions from an industrial facility might be chosen to be made in a wind direction for which there are no upwind sources in order to decrease this uncertainty.

The measurement route should ideally be as perpendicular to the wind direction as possible. Due to the  $\sin(\alpha_j)$  factor in equation (2.9), the flux calculation has the highest sensitivity to uncertainty in wind direction when  $\alpha_j$  is close to  $90^\circ$ .

As an emission plume travels further downwind from its source it spreads out, both in the horizontal direction and in the vertical direction. For wind measurement uncertainty reasons it is typically best to let the plume mix as high up as possible before measuring the flux. However, as the plume is dispersed in the horizontal direction, the size of columns will decrease, which increases the uncertainty due to background variations. The optimal downwind distance to measure is therefore a trade-off between these two effects and depends on the magnitude of the flux, the wind speed, how fast the plume is dispersed etc. In practice the choice of downwind distance is often severely limited by the existence of suitable measurement roads. Typical downwind distances for flux measurements of emissions from industries range from a few hundred meters to several kilometers. The optimal driving speed for flux measurements depends on a similar trade-off. Driving too slow increases uncertainties due to changes in wind and background concentrations that occur during the transect. Driving too fast while measuring a narrow plume will give a sparsely sampled plume, sometimes with only a couple of measurement points, also increasing the uncertainty. The quality of the road also affects how fast the measurement vehicle can be driven without vibrations affecting the spectroscopic measurements negatively. Measurement speeds between 30 and 70 km/h are typically used, but both slower and faster measurements are sometimes made.

## 2.3 Solar Occultation Flux

The mid-infrared wavelength region, approximately 2–20  $\mu\text{m}$  (500–5000  $\text{cm}^{-1}$ ), is widely used for molecular spectroscopy. The absorption lines in this region are due to excitations of vibrational energy levels, but rotational excitations are responsible for the fine structure. Bonds between certain combinations of atoms are associated with absorption in specific bands within the region, for instance molecules with C–H bonds typically have absorption lines in the region 2800–3000  $\text{cm}^{-1}$ . Apart from the bands associated with specific bonds, there is also a region called the fingerprint region, approximately 500–1500  $\text{cm}^{-1}$ , which is associated with bending vibrational modes. It is called the fingerprint region because many molecules have fairly unique absorption signatures in it, enabling more detailed speciation than the other bands.

Infrared spectra are generally measured with FTIR (Fourier Transform InfraRed) spectrometers, since they offer better signal-to-noise ratios than scanning monochromators due to Fellgett's advantage [15]. An FTIR spectrometer consists of a Michelson interferometer with a moving mirror at one of the arms. A detector records the intensity of the recombined light as the path difference is varied by the moving mirror. This intensity as a function of path length is called an interferogram. Since the intensity of light of a single wavenumber  $\nu$  is proportional

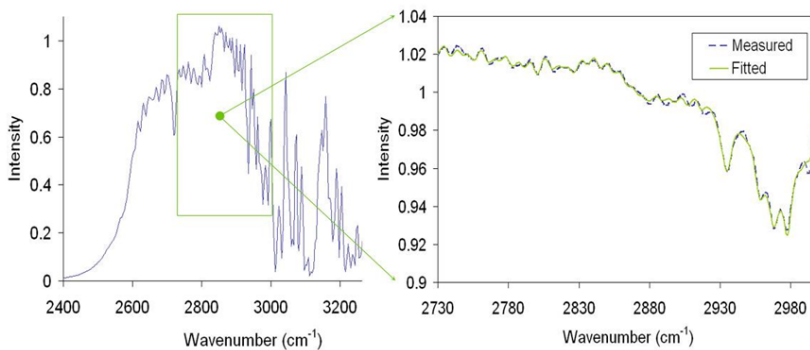


**Figure 2.3:** A measured solar spectrum is shown in the left, while the right plot shows the differential absorbance in the spectral retrieval window for alkanes together with the spectral fit from the spectral retrieval routine.

to  $1 + \cos(2\pi\nu d)$  after having passed the interferometer with path length  $d$ , the interferogram constitutes a Fourier cosine transform of the spectrum. By performing the corresponding inverse Fourier transform on the interferogram, the actual spectrum is obtained.

Atmospheric scattering is much weaker in the mid-infrared region than in the visible and ultraviolet regions. Thermal radiation from molecules and aerosols is basically the only radiation from a clear sky in this region, even in the middle of the day. This leaves direct sun light as the only practically useful natural light source for absorption spectroscopy in this region. The solar disk, however, only covers about  $0.5^\circ$  of the sky and it moves by approximately  $0.25^\circ/\text{minute}$ , so for spectroscopic measurements of direct sun light this motion must be tracked very carefully. Stationary high resolution infrared solar measurements are made within NDACC (Network for the Detection of Atmospheric Composition Change), a network of observatories to monitor long-term trends in atmospheric composition [16]. These typically employ a passive solar tracker that calculates the position of the sun based on their position, date and time of day and direct the field of view of the spectrometer with a set of mirrors in a mechanical device. Some of them also has an active step, which fine-tunes the measurement direction so that the light enters the spectrometer in the exact same direction at all times.

For direct sun measurements from a mobile platform, such as a measurement vehicle, a solar tracker is needed that cannot only track the sun's movement across the sky, but also compensate for the movement of the vehicle, due to turning, tilting, shocks and vibrations. This causes an apparent movement of the sun much greater and faster than the real one. For this purpose a purely active solar tracker was developed by the Optical remote sensing group [17] to facilitate flux measurements according to the principles described in section 2.2.

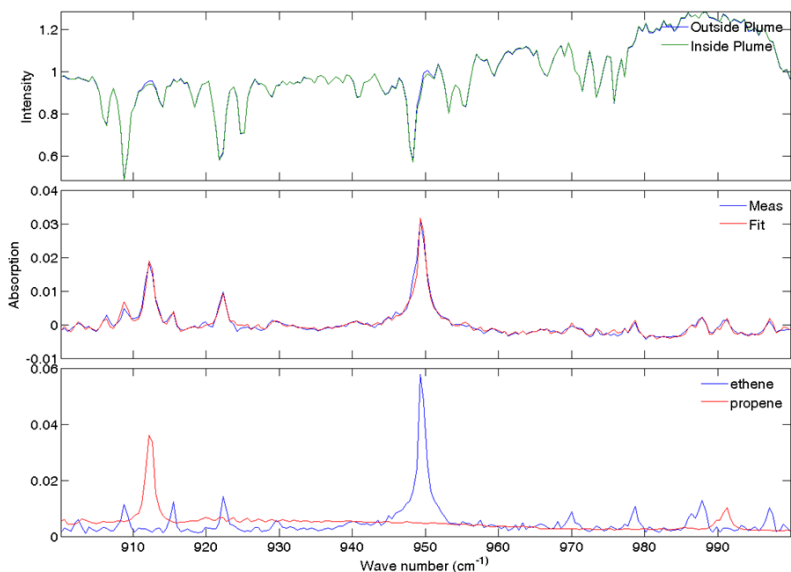


**Figure 2.4:** The top plot shows a spectrum measured in a plume as well as a reference spectrum measured outside the plume. The middle plot shows the differential absorbance between the two spectra and the fit of the alkene spectral retrieval routine. The lower plot shows the absorption cross sections of ethene and propene.

This method is called Solar Occultation Flux (SOF). Measurements of industrial emissions using this method have been made regularly since 2002, but the first peer-reviewed publication was. Similar measurements of volcanic emissions have also been made by [18, 19].

The strong absorption due to species present in the atmospheric background, primarily  $\text{H}_2\text{O}$  and  $\text{CO}_2$ , makes some wavelength regions unusable for SOF. This reduces the number of species that can practically be measured with SOF compared to similar absorption spectroscopy in a cell on the ground. In practice the number of species measurable is further reduced, since many species have too weak absorption cross sections or are not commonly present in large enough quantities in industrial plumes. So far, SOF measurements have mainly been performed in two spectroscopic modes. One mode is focused on the C–H bond absorption band around  $2700\text{--}3000\text{ cm}^{-1}$ . This is referred to as the alkane mode, since it allows spectral retrieval of an alkane mass column. This SOF mode and the alkane retrieval is described in detail in Paper III. A spectral fit from this retrieval is shown in figure 2.3. The second mode is focused on the fingerprint region and especially on the region between  $900$  and  $1000\text{ cm}^{-1}$ . In this region ethene ( $\text{C}_2\text{H}_4$ ), propene ( $\text{C}_3\text{H}_6$ ) and ammonia ( $\text{NH}_3$ ) are regularly measured with SOF, although many other could potentially be measured if they were present in large enough quantities. This mode is referred to as the alkene mode,

at least when measuring ethene and propene. This mode is described in detail in Paper I. A spectral fit of ethene and propene is shown in figure 2.4. Apart from the species described above, a few others have also been measured at times when they have been present in large enough quantities, such as 1,3-butadiene [20] and cyclohexane.

## 2.4 Mobile DOAS

Differential Optical Absorption Spectroscopy (DOAS) is a spectroscopic method used for measurements in the visible and ultraviolet wavelength regions. In this region molecular absorption is generally caused by excitations of valence electrons in the molecules. DOAS was originally developed by Perner and Platt [21–23] and has been used in a wide array of applications. A key difference between DOAS and infrared spectroscopy is the strong presence of scattering at these wavelengths. Rayleigh scattering by molecules is proportional to  $\lambda^{-4}$  and hence increases strongly with decreasing wavelength. Scattering out of the light path may be described by an additional term  $\varepsilon(\lambda)$  in Beer–Lambert’s law:

$$I_1(\lambda) = I_0(\lambda) \exp \left( - \sum_i \int_P n_i(\mathbf{x}) \sigma_i(\lambda, T, p) dl - \varepsilon(\lambda) \right) \quad (2.10)$$

This term represents both Rayleigh scattering, caused by molecules, and Mie scattering, caused by aerosols. It is heavily dependent on gas concentrations, aerosol loadings and path length, but these characteristics are not of much interest for DOAS purposes, since it is just an interfering term that needs to be compensated for. There are different ways to treat the scattering term in a spectral retrieval routine, but they are generally dependent on the fact that scattering varies slowly with wavelength compared to molecular absorption. One way to remove the scattering term is to apply a suitable high-pass filter to the absorbance spectra and to the cross sections, i.e. to both sides of equation (2.3). The high-pass filter removes both the slow-varying scattering and the slow-varying components of the cross sections, leaving only the fast-varying components of the cross sections. Another method is to include a polynomial in the spectral fitting routine and fit the coefficients of this polynomial along with the columns. The two methods can also be used in combination.

The strong scattering in the visible and ultraviolet region also has its advantages. The bright blue color of the clear sky in the middle of the day is a sign of how strong the scattering is in the visible region and although the intensity of this light is not as high as that of direct sun light, it can be used as light source for DOAS measurements. Since direct sun light is not needed, there is no need to track the position of the sun on the sky and it is possible to make sky measurements in virtually any direction. This fact is used in some DOAS variants to scan a cross section of the atmosphere angularly by gradually changing the

measurement direction [24–26]. The use of scattered light also enables measurements in cloudy conditions, although clouds may cause additional difficulties for the spectral retrieval leading to larger uncertainties.

One problem with measuring scattered light is that it is hard to know where the light has been scattered into the measurement path. The default assumption in sky-DOAS measurements is that the light measured was scattered into the light path in the stratosphere and then passes through the measured gas. However, scattering takes place continuously at all heights in the atmosphere so some of the light will also be scattered into the measurement path below and in the measured gas. This will cause a dilution of the absorption signal of the gas in the spectra which will result in retrieval of smaller columns. Additionally, in air masses with high aerosol loadings there may be multiple scattering, where light scatters back and forth many times causing a much longer path length in the air mass than if it would have passed right through. If such an air mass also contains significant amounts of the species measured, the retrieved columns of those species will be much larger than if the light had passed right through. The importance of these effects is dependent on the aerosol loadings, the height of the measured gas, clouds, the solar zenith angle, etc. Under certain circumstances they might be assumed to be negligible but in the general case radiative transfer modeling is needed to quantify and correct for them.

Another problem is caused by the presence of inelastic scattering in the incoming light. Rayleigh and Mie scattering are elastic forms of scattering, meaning they do not affect the wavelength of the scattered light. A fraction of the scattered light is, however, due to rotational Raman scattering, which causes small wavelength shifts. The result of this is a slight smoothing of the spectrum. This would not have been a significant problem if the incoming light had a smooth, slow-varying spectrum. The light from the sun, however, features deep absorption lines caused by gas in the outer regions of the sun. These lines are slightly filled in by inelastic scattering but not by elastic scattering. This would not matter if all the incoming light was inelastically scattered or if the proportions of elastic and inelastic scattering was constant. However, these proportions change with changing solar zenith angle and aerosol loadings. Dividing two spectra with different proportions of elastic and inelastic scattering results in a spectral structure that is similar to a molecular cross section, although it has no similar physical interpretation. This is called the Ring effect (discovered by Grainger and Ring [27]) and its spectrum is called a Ring spectrum. This effect can be corrected for by including a measured or synthesized Ring spectrum in the spectral fitting routine. If it is not corrected for, the Ring effect can cause spectral interference with the actual species evaluated, causing errors in the evaluated columns. A Ring spectrum can be synthesized from a high resolution solar spectrum. This spectrum is convolved with a function based on the theoretical rotational Raman scattering cross sections for  $N_2$  and  $O_2$ , the main constituents of the atmosphere, giving a high-resolution spectrum of the rotational Raman scattered light. The synthesized Ring spectrum is obtained by dividing this

spectrum with the original solar spectrum, after they have both been degraded to the instrument resolution. Fitting this spectrum along with the absorption cross sections in the spectral retrieval routine will give a first order correction of the Ring effect, which is typically sufficient.

Because spectral measurements in the visible and ultraviolet regions are often limited by statistical photon noise (or shot noise) and because array detectors are cheaply available, FTIR spectrometers do not have the same advantage as they have in the infrared region. The most common instrument is instead a Czerny-Turner spectrograph coupled with a CCD (Charge-Coupled Device) detector. A Czerny-Turner spectrograph consists of an entrance slit, a collimating mirror, a diffraction grating, and a focusing mirror. The slit limits the light entering the spectrometer to a narrow width, the first mirror collimates the light, the diffraction grating causes dispersion of light of different wavelengths, and the second mirror focuses the dispersed light on to the CCD. Each pixel, for a linear CCD, or each column, for a 2-dimensional CCD, will correspond to a specific wavelength of light and will detect the intensity for this wavelength. The wavelength interval can be adjusted by rotating the grating and the width of the interval can be changed by switching to a grating with a different grating constant.

A large number of species can potentially be measured with DOAS. However, as for SOF, the number of species typically encountered with large enough columns from industries to be measurable with Mobile DOAS is limited. Mobile DOAS has successfully been used to measure volcanic SO<sub>2</sub> emissions [24], emissions of SO<sub>2</sub>, NO<sub>2</sub> and HCHO from industrial areas [28, 29] as well as from entire cities [30–34]. The Mobile DOAS results presented in Paper **II** and Paper **III** are all based on spectral retrievals of SO<sub>2</sub>, NO<sub>2</sub> and formaldehyde (HCHO) from spectra measured in the wavelength interval 310–350 nm. SO<sub>2</sub> has been retrieved in the 310–325 nm window, while NO<sub>2</sub> and formaldehyde have been retrieved in the 324–350 nm window. Apart from the species of interest, the spectral retrievals have included two cross sections of O<sub>3</sub>, one at 223 K and one at 293 K, one for the (O<sub>2</sub>)<sub>2</sub> collision complex, and a synthesized Ring spectrum. The two cross sections for O<sub>3</sub> are needed to fit the absorption of both stratospheric and tropospheric ozone. The stratospheric column, however, is too large to allow quantification of the tropospheric ozone from this retrieval. The (O<sub>2</sub>)<sub>2</sub> collision complex is a hypothetical short-lived complex formed from collisions of oxygen molecules. It has never been detected chemically. The only evidence for it is a number of spectral absorption bands that are proportional to the square of the oxygen concentration. Even though it is proportional to the square of the concentration, the cross section can still be used in the spectral retrieval as a normal cross section, but the physical interpretation of it will be slightly different. The retrieved column of (O<sub>2</sub>)<sub>2</sub> can be used as an indicator of problems with multiple scattering. If the light that passes through a plume follows a similar path as the reference, there should not be a large differential (O<sub>2</sub>)<sub>2</sub> column between them. If there is significant multiple scattering in the plume, however,

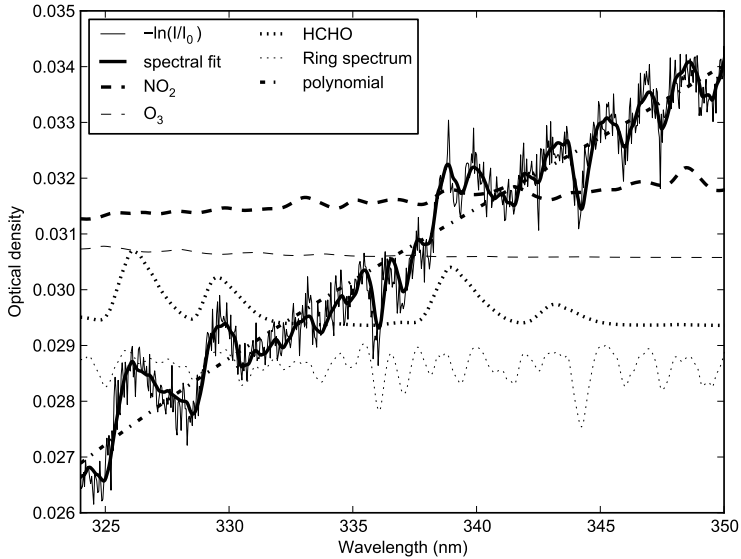


**Figure 2.5:** Spectral fit in the 324–350 nm retrieval window used for retrieval of  $\text{NO}_2$  and formaldehyde (HCHO) columns. The plot shows the measured and fitted absorbance, as well as the individual components of the fit. All the individual components except the polynomial have been shifted in the y-direction for the purpose of visual display.  $(\text{O}_2)_2$  was not included in the plot since it was negligible in size.

the total path length of the light will be different and the light will therefore pass through more  $(\text{O}_2)_2$ . A sudden large change in  $(\text{O}_2)_2$  when passing through a plume is hence a sign of multiple scattering in the plume. Figure 2.5 illustrates a spectral fit in the the 324–350 nm window. In this spectral fit, the reference was taken shortly before the evaluated spectrum. This explains why the  $\text{O}_3$  and  $(\text{O}_2)_2$  component are so small.

## 2.5 Wind measurements

As discussed in section 2.2, flux measurements with SOF and Mobile DOAS are fundamentally dependent on accurate wind velocity information. The wind velocity used in equation (2.9) should ideally be the mass-weighted average of the wind velocity of the gas measured in the plume cross section. This velocity is typically not possible to measure directly. Instead the goal must be to make wind measurements that are as representative as possible of the average velocity of the plume. A number of methods for wind measurements exist and are described below.

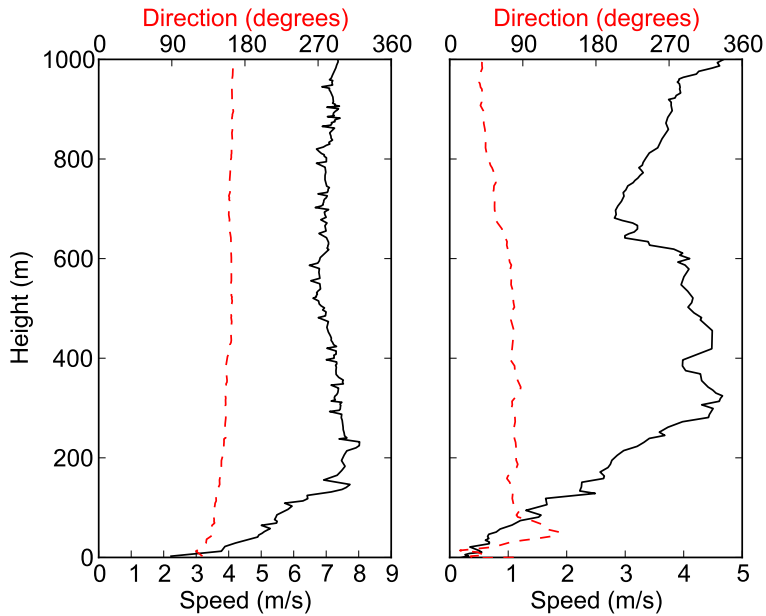


**Figure 2.6:** Two wind velocity profiles measured with radiosonde launches. The first wind speed profile is nearly constant over height with only a small decrease closest to the ground, while the second shows considerably more variation.

## 2.5.1 GPS radiosondes

A GPS radiosonde is a small electronic device powered with batteries. Its electronic components include a GPS (Global Positioning System) receiver, a radio transmitter, and various other sensors, such as temperature, pressure and relative humidity sensors. The sonde is launched from the ground with a large helium balloon and rises through the atmosphere with an ascent rate of a few meters per second. During the flight, the radiosonde sends its GPS position and other measurement data to a receiver on the ground, which logs the data. The balloon and radiosonde are assumed to follow the local horizontal wind field as they ascend the atmosphere, enabling a height profile of the wind velocity to be reconstructed by differentiating the horizontal position of the sonde with respect to time. The radiosondes used can easily reach altitudes well into the stratosphere and the additional sensors also give temperature, pressure and humidity profiles, but for the purpose of flux measurements, only the wind velocity profile in the boundary-layer, typically from ground up to 500–2000 m in fair weather, is of interest. Figure 2.6 shows the wind speed and wind direction profiles obtained from two radiosonde launches from a measurement campaign in Longview, Texas in May 2012. Each launch usually takes 5–10 minutes and gives a snapshot of the wind profile at that time. Since the radiosonde and balloon is

lost in each launch, the number of launches during a measurement campaign is often limited by budgetary constraints. For this reason, wind profiles measured with radiosondes sufficiently close in time are not always available for all flux measurements. For the purpose of flux calculations, the wind velocity is typically averaged over a height interval assumed to be representative of the height distribution of the gas in the plume. Height intervals used have been 0–200 m, 0–350 m, and 0–500 m. The averages calculated for these intervals have also been used as benchmarks for other measurements.

## **2.5.2 Ground-based wind masts**

Anemometers of different design, such as cup, windmill or sonic anemometers, mounted at the top of a weather mast is the cheapest way to make continuous wind measurements. Fixed installations of weather masts, operated by various organisations, often exist in many industrial locations, or in the vicinity. This wind data can often be obtained for free from the operator. A mobile mast can also be deployed at a suitable site. The problem with these wind measurements is that the wind field is more disturbed and turbulent closer to the ground. This means that the wind measurements from masts typically underestimate the wind speeds higher up significantly, but are also often subject to larger random variations. The magnitude of these effects depend on the height of the mast, its location, the surrounding topology, the speed and direction of the wind, etc. A higher mast means that the anemometer is further from the ground and the measurements suffer less from these effects, but higher masts are also more expensive and therefore less commonly available. To compensate for the systematically lower wind speeds measured by a mast, height interval averages of a large number of radiosonde profiles, as described above, can be compared to averages of the wind velocity measured by the mast during the same time interval. A scaling factor for the wind measured by the mast can then be determined so that they match on average. The flux calculations presented in Paper I, Paper II and Paper III have been made using radiosonde profiles when available sufficiently close in time, and mast measurements scaled to remove systematic differences compared to such radiosonde profiles.

## **2.5.3 Remote sensing wind profilers**

Remote sensing wind profilers in theory present the perfect combination of the advantages of both radiosondes and wind masts. They measure height profiles of the wind velocity continuously. The most common principle for this is to send a signal up into the atmosphere and measure the Doppler shift of the backscatter signal. This is typically done in a number of different directions to be able to calculate the different components of the wind. During a few SOF and Mobile DOAS measurement campaigns, wind profile data measured with radar and/or sodar profilers have been available. Radar profilers use electromagnetic waves in the radio frequency region, while sodar profilers use sound waves. However, these data generally had low availability and/or large errors compared to simultaneous

profiles measured by radiosondes. For this reason, they have not been used for flux calculations. To what extent these problems are inherent to the methods or just to the specific instruments or their operation is unclear. Recent progress for a third profiling method, wind lidars, which work according to the same principles using light in the near-infrared region, seems promising but so far costs are prohibitively high for these systems.

## 2.6 Error analysis

There are a number of different potential error sources for flux measurements with SOF and Mobile DOAS. In assessing them it is important to distinguish between systematic errors and random errors. Normally, several flux measurements are made on the same source and an average flux is calculated. If there is an uncorrelated random error with standard deviation  $\sigma$  in each flux measurement and the average of  $N$  such measurements is calculated, the error in the average will be  $\sigma/\sqrt{N}$ . For systematic errors, on the other hand, the size of the error does not decrease with the number of measurements. The potential error sources for flux measurements are listed below.

### 2.6.1 Spectroscopic errors

These are errors in flux measurements due to errors in spectroscopically determining the column along the measurement path.

#### Uncertainty in strength of cross sections

The cross section that have been used for SOF and Mobile DOAS have been measured and published by other groups. Cross sections are generally published together with an estimated uncertainty for the absolute strength. For VOC measurements with SOF, cross sections from PNNL (Pacific Northwest National Laboratory) [35], with reported uncertainties in the range 3–3.5%, have been used. For Mobile DOAS, cross section from Bogumil [36], Vandaele [37] and Cantrell [38] have been used for SO<sub>2</sub>, NO<sub>2</sub> and formaldehyde respectively. Their reported uncertainties are 2.8%, 4% and 3% respectively.

#### Retrieval errors

No spectral retrieval routine can fit the measured absorbance spectra perfectly. There will always be a residual left that could not be fitted. The residual has two types of causes, measurement noise and residual structures. Measurement noise will exist in any spectral measurement. In FTIR measurements detector noise is the dominant noise source, while in UV measurements with a CCD detector, statistical photon noise, also known as shot noise, will typically dominate. Both of these can approximately be described as uncorrelated Gaussian noise. For detector noise the signal-to-noise ratio is proportional to the light intensity, while for shot noise it is proportional to the square root of the intensity. If measurement noise is the only cause of the spectral fit residual, the residual will be mostly noise. Each fitted cross section will, however, receive some random inter-

ference from the noise, adding a random error to the evaluated columns. This error will also be a random uncorrelated error, whose magnitude can be statistically estimated from the magnitude of the residual noise and the strength of the cross section in the evaluation window. However, a simpler way to estimate the magnitude of the random column errors is to look at the random variations in evaluated column before or after passing the plume. The latter method is typically used to assess the random retrieval error.

Residual structures can be caused by any phenomenon affecting the measured spectra in a way that the spectral fitting routine cannot properly account for. Potential sources are unknown absorbers, scattering, changes in the instrument, non-linearity effects etc. These will generally produce residual components that are not noise, but instead has some non-random spectral structure. The effect of these on evaluated columns is more difficult to quantify. The effect will also generally not be a random error, but instead errors in consecutive measurements will be correlated. Some effects may cause a steady predictable drift in evaluated column, while others may just affect the measurements temporarily, causing a bump in the column time series.

## 2.6.2 Wind measurement errors

The largest source of error in flux measurements is generally the wind measurements. This is not primarily a measurement error, in the sense that the measured wind velocity is wrong, but in the sense that it is not representative of the wind velocity in the plume. This is mainly due to that the wind is not measured in the same location and/or at the same time as the gas in the plume. This could cause both systematic and random errors in both wind speed and wind direction.

### Wind speed errors

The main cause of systematic errors in wind speed is vertical wind gradients. These are caused by the wind field closer to the ground being retarded by the friction of the ground. This effect is somewhat mitigated by convection, which causes vertical mixing and smoothing of the vertical gradients. SOF and Mobile DOAS measurements are generally made during clear weather, associated with strong convection. Comparisons of averages of radiosonde wind speed profiles over the intervals 0–100 m, 0–200 m and 0–500 m were made for three different launch locations used in a measurement campaign in Houston in 2009 [39]. The wind speed in the interval 0–200 m was on average  $-3\%$ ,  $-9\%$  and  $+2\%$  compared to the 0–500 m interval for the three different launch sites. The same comparisons between the 0–100 m interval and 0–500 m showed average differences of  $-2\%$ ,  $-15\%$  and  $-1\%$ . During another campaign in Houston in 2006 [40] a similar comparison was made between the intervals 0–200 m and 0–500 m and the wind speed was found to be on average  $-6\%$  in the former compared to the latter. If these height intervals are thought to be representative of the variations in vertical extent among plumes measured with SOF and Mobile DOAS,

the systematic error due to not knowing the true plume extent will most likely be less than 10%.

The systematic difference between profile averages and winds measured by wind masts on the ground is often much larger, up to 30–40%. This is because the masts are so close to the ground in comparison. Most masts used in the Texas campaigns have been 10–20 m high. Emission plumes are however rarely confined to such low heights during daytime on sunny days. The same convection that smooths vertical wind gradients also causes rapid vertical mixing of the plume. Studies have showed typical vertical mixing speeds of 0.5–1.5 m/s [41]. For this reason, wind speeds measured by wind masts have been scaled to remove systematic differences compared to a radiosonde wind profiles in a chosen height interval, often 0–500 m. The remaining variation between profile averages and scaled wind mast speeds, typically has a standard deviation of 15–30%. Random errors can potentially be reduced by performing many measurements, but that is dependent on the random errors being uncorrelated. This might not always be guaranteed. If a certain type of wind measurement underestimates the speed of a plume during one measurement, it is probably likely to do so again if another measurement is made directly afterwards, but not if another measurement is made the next day. The random errors probably have some typical correlation scale, both in terms of time difference and distance. Since measurements are often made close in time after one another, the random error cannot necessarily be expected to be reduced by a factor of  $\sqrt{N}$ . For this reason the random error is used as a conservative estimate of the remaining wind speed error even after averaging several measurements.

### **Wind direction errors**

Systematic differences in wind directions may exist between different heights, although these differences are often less consistent than for wind speed. For wind masts on the ground there could be additional systematic errors in wind direction due to the local surrounding. The effect of wind direction errors on flux measurements is, however, not as straightforward as for wind speed. The wind direction enters the flux calculations, see equation (2.9), in the form of the factor  $\sin(\alpha_j)$  where  $\alpha_j$  is the angle between the wind direction and the driving direction of the measurement vehicle. An error in the wind direction will carry over to an error in  $\alpha_j$ , but its influence on the  $\sin(\alpha_j)$  will be highly dependent on  $\alpha_j$ . To estimate this effect, the average absolute error in wind direction has first been estimated by comparing wind mast measurements to radiosonde profiles, as done for the wind speed. The average absolute error for different wind masts has generally been in the interval 10–20°. The effect of this error has been approximated for different true values of  $\alpha_j$  by simulations assuming a Gaussian distribution of wind errors with standard deviation given by the average absolute errors of the wind masts. For  $\alpha_j = 90^\circ$  these simulations have shown average absolute flux errors in the range 4–8%, while for  $\alpha_j = 75^\circ$  this error has been in the range 8–12%. This is a random error but as for the random wind speed error

it cannot be assumed to be uncorrelated. For this reason 4–12% is a reasonable conservative estimate of the flux measurement error due to wind direction error. In many cases the larger wind speed errors can be avoided due to geometric constraints. If the location of the emission source is known, a straight line from the center of it to the center of the measured plume cross section should be a fairly good approximation of the wind direction. Measured wind directions that deviate too much from this should be avoided, either by choosing another wind source or by setting the wind direction manually. This practice should reduce the average wind direction error. This effect has, however, not been included in the estimate of the wind speed error.

### **2.6.3 Other error sources**

#### **Background variations**

In the ideal flux measurement the measured species are not present in the background atmosphere, and if they are, their concentration should at least be constant during the measurement. This is, however, not always the case. Background concentration can change due to upwind emission sources or changing air mass transport. This will cause deviations in the evaluated columns that are not due to the emissions in the plume. Furthermore, changes in the light path of the measured light can result in a longer or shorter path through a constant background concentration, also causing deviations in the evaluated columns. For SOF this change in light path is due to the movement of the sun, while for Mobile DOAS it is due changes in where light is scattered from. In many ways the effects of background variations are similar to those of residual structures. For this reason, they can be treated together. Both residual structures and background variations can sometimes result in steady, continuous increases or decreases in the evaluated columns. These can sometimes be compensated for by making a slant background correction, i.e. subtracting a linear function, or even a higher polynomial in some cases, from the column time series. But not all variations are steady and continuous. Sometimes these effects can cause large irregular baseline variations which cannot be compensated for. The relative error in a flux measurement due to baseline variations will depend on the size and type of the variations, the magnitude of the flux measured, and the width of the plume. The size of this error is generally limited by exclusion of measurements where the baseline variations would cause a too large error. For each flux measurement a baseline is established manually. If this cannot be established with reasonable certainty in relation to the magnitude of the plume peak, the measurement is rejected. Similarly, the measurement can also be rejected if the retrieval noise is too large in relation to the plume peak. It is estimated that this practice, as it has been applied, can limit the error due to baseline variations and retrieval noise to less than 10%.

## Plume meandering

The flux calculation formula assumes a stable plume remaining in the same place for the entire measurement. In reality the plume might often meander back and forth along the measurement route. The gas in the plume is primarily moving in the direction of the plume, not in the direction the plume is meandering. The drift of the plume is an apparent movement, caused by subsequent segments of the plume having been affected by slightly different wind fields, and thereby travelled along different trajectories. If this apparent plume drift is in the same direction as the measurement vehicle is driving, the plume will appear wider than it is, and if it is in the opposite direction it will appear narrower. If the measurement vehicle is driving with speed  $v$  and the apparent plume drift speed in parallel to the driving direction is  $u$ , the ratio between the calculated flux  $F_c$  and the true flux  $F_t$  will be:

$$\frac{F_c}{F_t} = \frac{v}{v - u} = \frac{1}{1 - \frac{u}{v}}. \quad (2.11)$$

If  $u$  is small compared to  $v$  this can be approximated by:

$$\frac{F_c}{F_t} = 1 + \frac{u}{v}. \quad (2.12)$$

Hence, the relative error in the flux calculation is  $u/v$  for small  $u$ . This assumes that the apparent plume drifts in the same direction with the same speed for the whole measurement. If it drifts back and forth within the time of one measurement, the effects will cancel and the error will be smaller. In the long run, a plume should be expected to drift equally in both directions. If several measurements are made on the same plume, drift along the driving direction should be equally likely as drift in the opposite direction. Hence, this error is assumed to be a random and uncorrelated error. Therefore, its magnitude should decrease with averaging of a large number of measurements. It is not known what typical drift speeds of plumes might be, but the effect is assumed to be small due to the moderate variations in flux typically seen between measurements and because of averaging.

### 2.6.4 Composite flux measurement error

The different error sources described above are assumed to be uncorrelated with each other and can therefore be combined to a composite flux measurement error,  $\sigma_c$ , by root-sum-square:

$$\sigma_c = \sqrt{\sum_i \sigma_i^2}, \quad (2.13)$$

where  $\sigma_i$  are the estimated standard deviations of the different error sources. In root-sum-squares the largest components tend to dominate, which for  $\sigma_c$  means that the wind speed error tends to be the most important. A wind error analysis has generally been made for each measurement campaign and a composite error or error interval has been calculated based on this. These values for  $\sigma_c$  have typically been in the range 20–40%. This error represents the error of an average of a number of measured fluxes compared to the average of the true fluxes at the times of those measurements. When using an average of measured fluxes as an estimate of emissions during a certain time period, there might also be sampling errors due to emissions at the times of the measurements not being representative of the time period.



# 3

## Summary of papers

### 3.1 Measurements of industrial emissions of alkenes in Texas using the solar occultation flux method

This paper presents the Solar Occultation Flux (SOF) method and its application to measure industrial alkene emissions. Results from SOF alkene measurements during the Second Texas Air Quality Study (TexAQS II) in 2006 are presented, both as a demonstration of the capabilities of the method, and to compare to emission inventories. SOF measurements of total emissions of ethene and propene from 7 sectors of Houston Ship Channel (HSC) as well as from the surrounding industrial areas in Bayport, Channelview, Chocolate Bayou, Freeport, Mont Belvieu, Sweeny and Texas City are presented and compared to emission inventory data for the corresponding areas. The geometrical average of the ratios between measured and inventory emissions for the different areas was 10.2 (+8, -5) for ethene and 11.7 (+7, -4) for propene. The two largest sources of alkene emissions were HSC and Mont Belvieu which had combined average measured ethene and propene emissions of  $1250 \pm 180$  kg/h and  $2140 \pm 520$  kg/h respectively. The corresponding 2006 inventory emissions for these areas were 145 and 181 kg/h.

Emissions from the area around Battleground Road were studied in detail due to their large temporal variations. In an episode on August 31, 2006, measured emissions rose from 684 to 2295 kg/h within 30 minutes, and then fell to only 237 kg/h within another 30 minutes. Hourly emission inventory data based on in-situ measurements showed large short-term variations in emissions from flares in this area, but these could not be shown to correlate exactly with the temporal

variations in emissions measurements. Still, the hourly inventory measurements showed the potential for large short-term variation in flare emissions, and not all flares in the area were included in the hourly inventory. Furthermore, the hourly inventory data for flares was based on the assumption of 98–99% combustion efficiency, and further large-scale variations might be expected if this assumption did not hold.

In a number of cases, emissions of alkenes were also estimated based on airborne measurement made in the same period. The airborne measurements indicated alkene emissions of up to 50% higher than those of SOF measurements made at the same time, but considering the uncertainties of the estimates based on the airborne measurements this may not be unreasonable. If anything, the airborne measurements would indicate that the SOF measurements underestimate the discrepancies between inventory emissions and actual emissions.

### **3.2 Quantitative measurements and modeling of industrial formaldehyde emissions in the Greater Houston area during campaigns in 2009 and 2011**

This paper investigates the occurrence of industrial sources of primary formaldehyde emissions in the Greater Houston area. The paper presents results from two measurement surveys using Mobile DOAS to detect and quantify local point sources of industrial formaldehyde emissions. The surveys were carried out in the largest conglomerates of refineries and petrochemical industries around Houston during measurement campaigns in 2009 and 2011. Five sources were repeatedly detected during the 2009 campaign, two in Texas City, two in Mont Belvieu and one in Houston Ship Channel. All except one of these were detected again during the 2011 campaign and two additional sources were found, one in Texas City and one in Houston Ship Channel. The average formaldehyde flux measured from these sources varied between 6 and 40 kg/h. The sum of the average emission measured from all sources was approximately 80 kg/h in 2009 and 130 kg/h in 2011. Since the surveys covered most large refineries and petrochemical facilities in the area, total primary formaldehyde emissions should not be expected to be drastically higher than these totals.

In 2009, ethene and propene emissions were measured with Solar Occultation Flux (SOF) in parallel to the Mobile DOAS measurements of formaldehyde during large parts of the survey. Thirteen cases were identified where the formaldehyde plume from one of these sources was detected together with a significant plume of ethene, propene or both. These were selected for investigation if the formaldehyde emissions could be explained by oxidation of the alkenes. For this purpose a Lagrangian photochemical plume model was used to simulate the plume chemistry for the thirteen cases. In addition to the ethene, propene and formaldehyde emissions, fluxes of alkanes measured with SOF and of NO<sub>2</sub> and

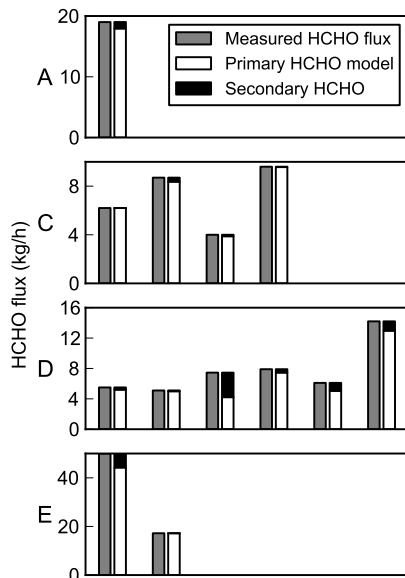


**Figure 3.1:** Measured HCHO fluxes for the 13 plume chemistry simulation cases and the fraction of it explained by primary and secondary emissions respectively according to the results. The cases are sorted by the emission source (labeled A, C, D and E) from which the plume was detected.

SO<sub>2</sub> measured with Mobile DOAS were used as input data for the model in cases where they were detected. Measurement made at Moody Tower on the University of Houston campus as part of the SHARP campaign were also used as input. The results of the simulations are shown in figure 3.1. In one case, the plume chemistry model could assign as much as 43% of the formaldehyde flux to secondary emissions, but in most cases this fraction was lower than 10%.

A sensitivity analysis of the plume chemistry was performed to investigate which potential errors in the input data could have a meaningful effect on the outcome of the simulations. This showed that the parameters the model was most sensitive to was the wind speed, the vertical mixing speed and whether or not included alkane and NO<sub>x</sub> were assumed to be coming from the same source as the formaldehyde and alkenes. Even with these parameters optimized for formaldehyde production within realistic constraints, the model could not explain more than a small fraction of the formaldehyde as secondary in most cases. From this it was concluded that most of the formaldehyde from the sources detected in these surveys was primary emissions. However, due to the large industrial emis-

sions of ethene and propene in the Houston area measured in these and other campaigns, secondary formaldehyde is still thought to dominate over primary emissions further downwind from emission sources.

### **3.3 Emission measurements of alkenes, alkanes, SO<sub>2</sub> and NO<sub>2</sub> from stationary sources in Southeast Texas over a 5-year-period using SOF and Mobile DOAS**

In this paper results from SOF (Solar Occultation Flux) and Mobile DOAS measurements industrial emissions of alkanes, alkenes (ethene and propene), SO<sub>2</sub> and NO<sub>2</sub> from four measurement campaigns in Southeast and East Texas are presented together to give an overview. The campaigns were carried out in four different years, 2006, 2009, 2011 and 2012, and partly overlapped in geographical coverage, mainly in that the three first studies were all heavily focused on the Greater Houston area. This allowed for comparisons between the different areas as well as from year to year. The largest difference from one year to another was seen in the alkene emissions from Houston Ship Channel (HSC). In 2006 the average ethene emission from HSC was approximately 1500 kg/h and propene emissions were almost 900 kg/h on average. In 2009 the same numbers had dropped to roughly 600 kg/h for both species and in 2011 the emissions remained on similar level. Large variations were seen in the alkene fluxes measured from HSC in 2006, which suggests that the measurements were influenced by upset emissions. In that case the upset emissions could also be the explanation for the large difference between 2006 and 2009. Apart from this VOC emissions were surprisingly stable over the years. The alkane emissions from HSC, for instance, were within 10% of 11,500 kg/h during 2006, 2009 and 2011.

The measured emissions were all compared to reported annual average emissions for the corresponding areas. Emissions reported by the industries were extracted from the State of Texas Air Reporting System (STARS) and compiled by area and species. Measured alkane emissions were compared to reported emissions speciated as specific alkanes, unspecified alkanes, alcohols or broad categories that can be assumed to be dominated by alkanes, such as crude oil and naphtha. Ethene, propene and SO<sub>2</sub> could on the other hand be compared to their direct equivalent in the emission inventories. NO<sub>2</sub> was compared to emissions reported as either NO, NO<sub>2</sub> or NO<sub>x</sub>, but NO<sub>x</sub> was the most common speciation. According to airborne measurements during the 2006 campaign the typical NO<sub>2</sub> to NO<sub>x</sub> ratio during the Mobile DOAS measurements was 0.75. In figure 3.2, the ratios between the average emission measured and the annual average emission reported have been calculated and plotted for each campaign, and the areas and species that were measured in that campaign. This highlights the broad pattern that measured VOC emissions, both alkanes and alkenes, are typically 5–15

times larger than the corresponding reported emissions, while measured  $\text{SO}_2$  and  $\text{NO}_2$  emissions generally are closer to reported emissions, with typical ratios of 0.5–2. This pattern holds fairly well for most areas and years. It is argued that current methods for estimating emissions employed by industries might broadly underestimate the actual emissions for VOCs but not for  $\text{SO}_2$  and  $\text{NO}_2$ , due to larger uncertainties inherent to VOC emission mechanisms.

Additionally, the article investigates the possibility that measured VOC emission might be significantly unrepresentative of annual emissions due to the impact of the unrepresentative meteorological conditions during the measurements on evaporative losses. This is done by applying emission factor formulas from AP-42 to two example storage tanks, one external floating roof tank storing crude oil and one internal floating roof tank storing gasoline. These were chosen to represent the most common units in a refinery with significant meteorological effects in the emissions factor formulas. Emissions were estimated for these tanks using annual averages of temperatures, solar radiations and wind speeds measured in HSC as well as similar averages over just the campaign periods and over just the daytime hours in the days with measurements. Based on this, upper estimates of the effect of unrepresentative meteorological winds were in the interval 34–44% in all cases except the external floating roof tank during the 2011 campaign, in which the effect was estimated to be up to 90%. This was due to the exceptionally strong wind during that campaign which according to the emissions factor formulas has strong effects on external floating roof tanks. These effects are, however, too small to explain the discrepancies seen between measured and reported alkane emissions.

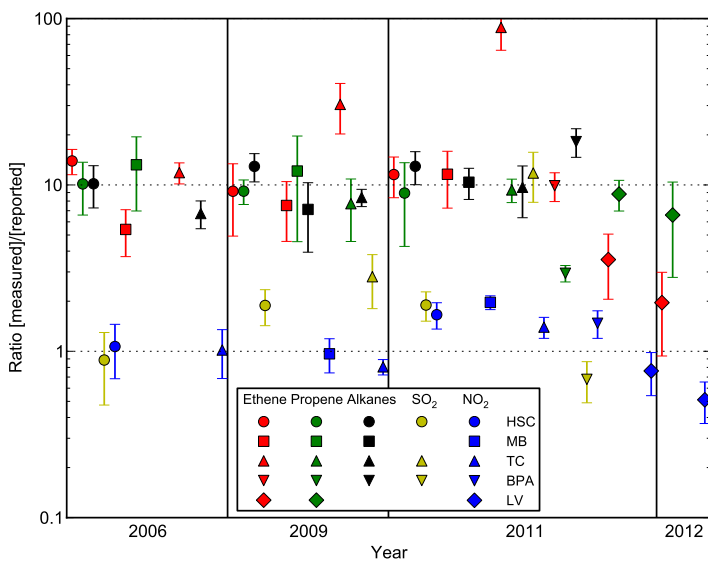


**Figure 3.2:** Ratios of emissions measured with SOF and Mobile DOAS to annual average emissions reported to State of Texas Air Reporting System (STARS) for each year, species and area. Circle markers are used for Houston Ship Channel (HSC), squares for Mont Belvieu (MB), upward triangles for Texas City (TC), downward triangles for Beaumont/Port Arthur (BPA) and diamonds for Longview (LV). Red markers are used for ethene, green for propene, black for alkanes, yellow for SO<sub>2</sub> and blue for NO<sub>2</sub>. The markers indicate the ratio of the mean of all flux measurements to the reported emissions, while the error bars indicate ratio of the mean plus/minus one standard deviation to the reported emissions. The error bars only represent the variation in the flux measurements, not uncertainty in measurements or in reported emissions. The x-scale only indicate the year of the measurements; the x-position within a year has no meaning. Reported emissions for 2011 were used for the 2012 ratios since 2012 data was not yet available.

# Bibliography

- [1] J. A. De Gouw, S. Te Lintel Hekkert, J. Mellqvist, C. Warneke, E. L. Atlas, F. C. Fehsenfeld, A. Fried, G. J. Frost, F. J. M. Harren, J. S. Holloway, B. Lefer, R. Lueb, J. F. Meagher, D. D. Parrish, M. Patel, L. Pope, D. Richter, C. Rivera, T. B. Ryerson, J. Samuelsson, J. Walega, R. A. Washenfelder, P. Weibring, and X. Zhu. Airborne measurements of ethene from industrial sources using laser photo-acoustic spectroscopy. *Environmental Science and Technology*, 43(7):2437–2442, 2009.
- [2] B. T. Jobson, C. M. Berkowitz, W. C. Kuster, P. D. Goldan, E. J. Williams, F. C. Fehsenfeld, E. C. Apel, T. Karl, W. A. Lonneman, and D. Riemer. Hydrocarbon source signatures in Houston, Texas: Influence of the petrochemical industry. *Journal of Geophysical Research D: Atmospheres*, 109(24):1–26, 2004.
- [3] T. Karl, T. Jobson, W. C. Kuster, E. Williams, J. Stutz, R. Shetter, S. R. Hall, P. Goldan, F. Fehsenfeld, and W. Lindinger. Use of proton-transfer-reaction mass spectrometry to characterize volatile organic compound sources at the La Porte super site during the Texas Air Quality Study 2000. *Journal of Geophysical Research D: Atmospheres*, 108(16):ACH 13–1 – ACH 13–15, 2003.
- [4] L. I. Kleinman, P. H. Daum, D. Imre, Y. N. Lee, L. J. Nunnermacker, S. R. Springston, J. Weinstein-Lloyd, and J. Rudolph. Ozone production rate and hydrocarbon reactivity in 5 urban areas: A cause of high ozone concentration in Houston. *Geophysical Research Letters*, 29(10):105–1–105–4, 2002.
- [5] D. D. Parrish, D. T. Allen, T. S. Bates, M. Estes, F. C. Fehsenfeld, G. Feingold, R. Ferrare, R. M. Hardesty, J. F. Meagher, J. W. Nielsen-Gammon, R. B. Pierce, T. B. Ryerson, J. H. Seinfeld, and E. J. Williams. Overview of the second texas air quality study (TexAQSS II) and the Gulf of Mexico atmospheric composition and climate study (GoMACCS). *Journal of Geophysical Research D: Atmospheres*, 114(13), 2009.

- [6] T. B. Ryerson, M. Trainer, W. M. Angevine, C. A. Brock, R. W. Dissly, F. C. Fehsenfeld, G. J. Frost, P. D. Goldan, J. S. Holloway, G. Hübler, R. O. Jakoubek, W. C. Kuster, J. A. Neuman, D. K. Nicks Jr, D. D. Parrish, J. M. Roberts, D. T. Sueper, E. L. Atlas, S. G. Donnelly, F. Flocke, A. Fried, W. T. Potter, S. Schauffler, V. Stroud, A. J. Weinheimer, B. P. Wert, C. Wiedinmyer, R. J. Alvarez, R. M. Banta, L. S. Darby, and C. J. Senff. Effect of petrochemical industrial emissions of reactive alkenes and NO<sub>x</sub> on tropospheric ozone formation in Houston, Texas. *Journal of Geophysical Research D: Atmospheres*, 108(8):ACH 8–1 – ACH 8–24, 2003.
- [7] R. A. Washenfelder, M. Trainer, G. J. Frost, T. B. Ryerson, E. L. Atlas, J. A. De Gouw, F. M. Flocke, A. Fried, J. S. Holloway, D. D. Parrish, J. Peischl, D. Richter, S. M. Schauffler, J. G. Walega, C. Warneke, P. Weibring, and W. Zheng. Characterization of NO<sub>x</sub>, SO<sub>2</sub>, ethene, and propene from industrial emission sources in Houston, Texas. *Journal of Geophysical Research D: Atmospheres*, 115(16), 2010.
- [8] B. P. Wert, M. Trainer, A. Fried, T. B. Ryerson, B. Henry, W. Potter, W. M. Angevine, E. Atlas, S. G. Donnelly, F. C. Fehsenfeld, G. J. Frost, P. D. Goldan, A. Hansel, J. S. Holloway, G. Hubler, W. C. Kuster, D. K. Nicks Jr, J. A. Neuman, D. D. Parrish, S. Schauffler, J. Stutz, D. T. Sueper, C. Wiedinmyer, and A. Wisthaler. Signatures of terminal alkene oxidation in airborne formaldehyde measurements during TexAQS 2000. *Journal of Geophysical Research D: Atmospheres*, 108(3):ACH 8–1 – ACH 8–14, 2003.
- [9] Jessica B. Gilman, William C. Kuster, Paul D. Goldan, Scott C. Herndon, Mark S. Zahniser, Sara C. Tucker, W. Alan Brewer, Brian M. Lerner, Eric J. Williams, Robert A. Harley, Fred C. Fehsenfeld, Carsten Warneke, and Joost A. de Gouw. Measurements of volatile organic compounds during the 2006 TexAQS/GoMACCS campaign: Industrial influences, regional characteristics, and diurnal dependencies of the OH reactivity. *Journal of Geophysical Research: Atmospheres*, 114(D7), 2009.
- [10] S. W. Kim, S. A. McKeen, G. J. Frost, S. H. Lee, M. Trainer, A. Richter, W. M. Angevine, E. Atlas, L. Bianco, K. F. Boersma, J. Brioude, J. P. Burrows, J. De Gouw, A. Fried, J. Gleason, A. Hilboll, J. Mellqvist, J. Peischl, D. Richter, C. Rivera, T. Ryerson, S. Te Lintel Hekkert, J. Walega, C. Warneke, P. Weibring, and E. Williams. Evaluations of NO<sub>x</sub> and highly reactive VOC emission inventories in Texas and their implications for ozone plume simulations during the Texas Air Quality Study 2006. *Atmospheric Chemistry and Physics*, 11(22):11361–11386, 2011.
- [11] D. D. Parrish, T. B. Ryerson, J. Mellqvist, J. Johansson, A. Fried, D. Richter, J. G. Walega, R. A. Washenfelder, J. A. De Gouw, J. Peischl,

- K. C. Aikin, S. A. McKeen, G. J. Frost, F. C. Fehsenfeld, and S. C. Herndon. Primary and secondary sources of formaldehyde in urban atmospheres: Houston Texas region. *Atmospheric Chemistry and Physics*, 12(7):3273–3288, 2012.
- [12] B. Buzcu Guven and E. P. Olaguer. Ambient formaldehyde source attribution in Houston during TexAQS II and TRAMP. *Atmospheric Environment*, 45(25):4272–4280, 2011.
- [13] S. Friedfeld, M. Fraser, K. Ensor, S. Tribble, D. Rehle, D. Leleux, and F. Tittel. Statistical analysis of primary and secondary atmospheric formaldehyde. *Atmospheric Environment*, 36(30):4767–4775, 2002.
- [14] B. Rappenglück, P. K. Dasgupta, M. Leuchner, Q. Li, and W. Luke. Formaldehyde and its relation to CO, PAN, and SO<sub>2</sub> in the Houston-Galveston airshed. *Atmospheric Chemistry and Physics*, 10(5):2413–2424, 2010.
- [15] P. B. Fellgett. On the Ultimate Sensitivity and Practical Performance of Radiation Detectors. *J. Opt. Soc. Am.*, 39(11):970–976, Nov 1949.
- [16] J. Mellqvist, B. Galle, T. Blumenstock, F. Hase, D. Yashcov, J. Notholt, B. Sen, J.-F. Blavier, G. C. Toon, and M. P. Chipperfield. Ground-based FTIR observations of chlorine activation and ozone depletion inside the Arctic vortex during the winter of 1999/2000. *Journal of Geophysical Research: Atmospheres*, 107(D20):SOL 6–1–SOL 6–16, 2002.
- [17] Manne Kihlman. *Application of Solar FTIR spectroscopy for quantifying gas emissions*. PhD thesis, Chalmers Univeristy of Technology, 2005.
- [18] Hayley Duffell, Clive Oppenheimer, and Mike Burton. Volcanic gas emission rates measured by solar occultation spectroscopy. *Geophysical Research Letters*, 28(16):3131–3134, 2001.
- [19] P. Weibring, J. Swartling, H. Edner, S. Svanberg, T. Caltabiano, D. Condarelli, G. Cecchi, and L. Pantani. Optical monitoring of volcanic sulphur dioxide emissions - comparison between four different remote-sensing spectroscopic techniques. *Optics and Lasers in Engineering*, 37(2 - 3):267 – 284, 2002.
- [20] J. K. E. Johansson, J. Mellqvist, J. Samuelsson, B. Offerle, B. Rappenglück, D. Anderson, B. Lefer, S. Alvarez, and J. Flynn. Quantification of industrial emissions of VOCs, NO<sub>2</sub> and SO<sub>2</sub> by SOF and Mobile DOAS. Technical Report 10-006, AQRP, 2011.
- [21] D. Perner, D. H. Ehhalt, H. W. Pätz, U. Platt, E. P. Röth, and A. Volz. OH - Radicals in the lower troposphere. *Geophysical Research Letters*, 3(8):466–468, 1976.

- [22] D. Perner and U. Platt. Detection of nitrous acid in the atmosphere by differential optical absorption. *Geophysical Research Letters*, 6(12):917–920, 1979.
- [23] U. Platt, D. Perner, and H. W. Pätz. Simultaneous measurement of atmospheric CH<sub>2</sub>O, O<sub>3</sub>, and NO<sub>2</sub> by differential optical absorption. *Journal of Geophysical Research: Oceans*, 84(C10):6329–6335, 1979.
- [24] B. Galle, C. Oppenheimer, A. Geyer, A. J. S. McGonigle, M. Edmonds, and L. Horrocks. A miniaturised ultraviolet spectrometer for remote sensing of SO<sub>2</sub> fluxes: A new tool for volcano surveillance. *Journal of Volcanology and Geothermal Research*, 119(1-4):241–254, 2002.
- [25] M. Edmonds, R.A. Herd, B. Galle, and C.M. Oppenheimer. Automated, high time-resolution measurements of SO<sub>2</sub> flux at Soufrière Hills Volcano, Montserrat. *Bulletin of Volcanology*, 65(8):578–586, 2003.
- [26] A. J. S. McGonigle, C. Oppenheimer, A. R. Hayes, B. Galle, M. Edmonds, T. Caltabiano, G. Salerno, M. Burton, and T. A. Mather. Sulphur dioxide fluxes from Mount Etna, Vulcano, and Stromboli measured with an automated scanning ultraviolet spectrometer. *Journal of Geophysical Research: Solid Earth*, 108(B9), 2003.
- [27] J. F. Grainger and J. Ring. Anomalous Fraunhofer Line Profiles. *Nature*, 193(4817):762–762, feb 1962.
- [28] C. Rivera, G. Sosa, H. Wöhrnschimmel, B. De Foy, M. Johansson, and B. Galle. Tula industrial complex (Mexico) emissions of SO<sub>2</sub> and NO<sub>2</sub> during the MCMA 2006 field campaign using a mobile mini-DOAS system. *Atmospheric Chemistry and Physics*, 9(17):6351–6361, 2009.
- [29] C. Rivera, J. Mellqvist, J. Samuelsson, B. Lefer, S. Alvarez, and M. R. Patel. Quantification of NO<sub>2</sub> and SO<sub>2</sub> emissions from the houston ship channel and texas city industrial areas during the 2006 texas air quality study. *Journal of Geophysical Research D: Atmospheres*, 115(8), 2010.
- [30] M. Johansson, B. Galle, T. Yu, L. Tang, D. Chen, H. Li, J. X. Li, and Y. Zhang. Quantification of total emission of air pollutants from Beijing using mobile mini-DOAS. *Atmospheric Environment*, 42(29):6926–6933, 2008.
- [31] M. Johansson, C. Rivera, B. DeFoy, W. Lei, J. Song, Y. Zhang, B. Galle, and L. Molina. Mobile mini-DOAS measurement of the outflow of NO<sub>2</sub> and HCHO from Mexico City. *Atmospheric Chemistry and Physics*, 9(15):5647–5653, 2009.
- [32] O. Ibrahim, R. Shaiganfar, R. Sinreich, T. Stein, U. Platt, and T. Wagner. Car MAX-DOAS measurements around entire cities: Quantification of

- NOx emissions from the cities of Mannheim and Ludwigshafen (Germany). *Atmospheric Measurement Techniques*, 3(3):709–721, 2010.
- [33] T. Wagner, O. Ibrahim, R. Shaiganfar, and U. Platt. Mobile MAX-DOAS observations of tropospheric trace gases. *Atmospheric Measurement Techniques*, 3(1):129–140, 2010.
- [34] R. Shaiganfar, S. Beirle, M. Sharma, A. Chauhan, R. P. Singh, and T. Wagner. Estimation of NOx emissions from Delhi using Car MAX-DOAS observations and comparison with OMI satellite data. *Atmospheric Chemistry and Physics*, 11(21):10871–10887, 2011.
- [35] Steven W. Sharpe, Timothy J. Johnson, Robert L. Sams, Pamela M. Chu, George C. Rhoderick, and Patricia A. Johnson. Gas-Phase Databases for Quantitative Infrared Spectroscopy. *Applied Spectroscopy*, 58(12):1452–1461, 2004.
- [36] K. Bogumil, J. Orphal, T. Homann, S. Voigt, P. Spietz, O. C. Fleischmann, A. Vogel, M. Hartmann, H. Kromminga, H. Bovensmann, J. Frerick, and J. P. Burrows. Measurements of molecular absorption spectra with the SCIAMACHY pre-flight model: instrument characterization and reference data for atmospheric remote-sensing in the 230-2380 nm region. *Journal of Photochemistry and Photobiology A: Chemistry*, 157(2-3):167–184, 5/5/ 2003.
- [37] A. C. Vandaele, C. Hermans, P. C. Simon, M. Carleer, R. Colin, S. Fally, M. F. Mérienne, A. Jenouvrier, and B. Coquart. Measurements of the NO<sub>2</sub> absorption cross-section from 42 000 cm<sup>-1</sup> to 10 000 cm<sup>-1</sup> (238-1000 nm) at 220 K and 294 K. *Journal of Quantitative Spectroscopy and Radiative Transfer*, 59(3-5):171–184, 1998.
- [38] C. A. Cantrell, J. A. Davidson, A. H. McDaniel, R. E. Shetter, and J. G. Calvert. Temperature-dependent formaldehyde cross sections in the near-ultraviolet spectral region. *Journal of Physical Chemistry*, 94(10):3902–3908, 1990.
- [39] J. Mellqvist, J. K. E. Johansson, J. Samuelsson, B. Offerle, B. Rappenglück, C.-S. Wilmot, and R. Fuller. Investigation of VOC radical sources in the Houston area by the Solar Occultation Flux (SOF) method, mobile DOAS (SOF-II) and mobile extractive FTIR. Technical report, TERC, 2010.
- [40] J. Mellqvist, J. Samuelsson, C. Rivera, B. Lefer, and M. Patel. Measurements of industrial emissions of VOCs, NH<sub>3</sub>, NO<sub>2</sub> and SO<sub>2</sub> in Texas using the Solar Occultation Flux method and mobile DOAS. Technical report, HARC, 2007.

- [41] S. C. Tucker, W. A. Brewer, R. M. Banta, C. J. Senff, S. P. Sandberg, D. C. Law, A. M. Weickmann, and R. M. Hardesty. Doppler lidar estimation of mixing height using turbulence, shear, and aerosol profiles. *Journal of Atmospheric and Oceanic Technology*, 26(4):673–688, 2009.